Computers in Biology and Medicine 145 (2022) 105439

Contents lists available at ScienceDirect

Computers in Biology and Medicine

journal homepage: www.elsevier.com/locate/compbiomed

Crystal structure of Acetyl-CoA carboxylase (AccB) from *Streptomyces antibioticus* and insights into the substrate-binding through *in silico mutagenesis* and biophysical investigations

Imtiaz Ali [a], Abbas Khan [b], Zhang Fa [a], Taimoor Khan [b], Dong-Qing Wei [b,c,d], Jianting Zheng [a,e,*]

[a] State Key Laboratory of Microbial Metabolism, School of Life Sciences and Biotechnology, Shanghai Jiao Tong University, Shanghai, 200240, PR China
[b] Department of Bioinformatics and Biological Statistics, School of Life Sciences and Biotechnology, Shanghai Jiao Tong University, Shanghai, 200240, PR China
[c] State Key Laboratory of Microbial Metabolism, Shanghai-Islamabad-Belgrade Joint Innovation Center on Antibacterial Resistances, Joint Laboratory of International Cooperation in Metabolic and Developmental Sciences, Ministry of Education and School of Life Sciences and Biotechnology, Shanghai Jiao Tong University, Shanghai, 200030, PR China
[d] Peng Cheng Laboratory, Vanke Cloud City Phase I Building 8, Xili Street, Nashan District, Shenzhen, Guangdong, 518055, PR China
[e] Joint International Research Laboratory of Metabolic & Developmental Sciences, Shanghai Jiao Tong University, Shanghai, PR China

ARTICLE INFO

Keywords:
Streptomyces antibioticus
Acetyl-CoA carboxylase
Carboxyl transferase
Substrate binding
MD simulation

ABSTRACT

Acetyl-CoA carboxylase (ACC) is crucial for polyketides biosynthesis and acts as an essential metabolic checkpoint. It is also an attractive drug target against obesity, cancer, microbial infections, and diabetes. However, the lack of knowledge, particularly sequence-structure function relationship to narrate ligand-enzyme binding, has hindered the progress of ACC-specific therapeutics and unnatural "natural" polyketides. Structural characterization of such enzymes will boost the opportunity to understand the substrate binding, designing new inhibitors and information regarding the molecular rules which control the substrate specificity of ACCs. To understand the substrate specificity, we determined the crystal structure of AccB (Carboxyl-transferase, CT) from *Streptomyces antibioticus* with a resolution of 2.3 Å and molecular modeling approaches were employed to unveil the molecular mechanism of acetyl-CoA recognition and processing. The CT domain of *S. antibioticus* shares *a* similar structural organization with the previous structures and the two steps reaction was confirmed by enzymatic assay. Furthermore, to reveal the key hotspots required for the substrate recognition and processing, *in silico* mutagenesis validated only three key residues (V223, Q346, and Q514) that help in the fixation of the substrate. Moreover, we also presented atomic level knowledge on the mechanism of the substrate binding, which unveiled the terminal loop (500–514) function as an opening and closing switch and pushes the substrate inside the cavity for stable binding. A significant decline in the hydrogen bonding half-life was observed upon the alanine substitution. Consequently, the presented structural data highlighted the potential key interacting residues for substrate recognition and will also help to re-design ACCs active site for proficient substrate specificity to produce diverse polyketides.

1. Introduction

Acyl–CoA carboxylases (ACCs) include propionyl-CoA carboxylase (PCC) and acetyl-CoA carboxylase (ACC), which catalyzes the first committed step of providing building blocks during synthesis of complex lipids, fatty acids, and polyketides natural products [1] including antibiotics, anticancer, antifungal, immunosuppressant and blood-pressure-lowering compounds [2]. Mechanistically, these enzymes complexes catalyze the carboxylation of α carbon of three substrates; acetyl-CoA, propionyl-CoA, or butyryl-CoA producing malonyl, methyl-malonyl, or ethyl-malonyl-CoA, respectively [3,4]. During the reaction, ACC accepts acetyl-CoA as the preferred substrate, while propionyl-CoA carboxylase (PCC) preferentially utilizes propionyl-CoA. In yeast, mammalian and eukaryotic cells, ACCs contain all the three subunits in a single polypeptide chain (homomeric form) and function as a large multifunctional enzyme. In contrast, *Escherichia*

* Corresponding author. State Key Laboratory of Microbial Metabolism, School of Life Sciences and Biotechnology, Shanghai Jiao Tong University, Shanghai, 200240, PR China.
E-mail address: jtzheng@sjtu.edu.cn (J. Zheng).

https://doi.org/10.1016/j.compbiomed.2022.105439
Received 4 December 2021; Received in revised form 14 March 2022; Accepted 20 March 2022
Available online 23 March 2022

coli and most of plastids ACCs (heteromeric form) are composed of independent subunits, including biotin-carboxyl carrier protein (BCCP), biotin-carboxylase (BC), and carboxyltransferase (CT) [3,5]. Similarly, most ACCs in actinomycetes consists of three subunits: α-subunit containing the BCCP and BC domain, β-subunit confined to the CT domain, and an ε-subunit, which enhances enzyme activity and also serves as the adapter between the two (α and β) subunits [6]. The ACCs carboxylation is a two-step reaction with ATP-dependent carboxy-biotin production followed by the carboxyl moiety transfer to acetyl-CoA. In mammals, a single protein catalyzes both reactions, while in prokaryotes, both steps are regulated by the three main functional domains. This involves regulation of the first reaction catalyzed by the BC domain [7] located in the N-terminal of α subunit to form carboxy-biotin. It is followed by BCCP, present on the C- terminus of α subunit to attach the co-factor biotin like a "swinging arm" [1,8]. The second reaction is catalyzed by the β subunit termed as CT domain, which facilitates the transfer of carboxyl group from carboxy-biotin to propionyl- or acetyl- CoA and forms methyl-malonyl- or malonyl-CoA [9].

Malonyl-CoA is the product of ACC-catalyzed reaction, which is not limited to its starring role as a substrate for fatty acid synthesis. It also allosterically inhibits the enzyme called carnitine palmitoyltransferase I (CPT-I), which catalyzes the first step in the oxidation of mitochondrial fatty acids [10,11]. Malonyl-CoA has an important regulatory role in the control of mitochondrial fatty acids uptake. It serves as a metabolic signal to control fatty acid production under altered nutritional requirements and dietary changes in animals. The importance of this cellular product is also reflected by acting as a modulating switch between fatty acid utilization and carbohydrates in skeletal muscles and the liver [12]. Genetic and pharmacological studies strongly support the importance of ACCs as a drug sighting target to lower triglycerides by stimulating fatty acid oxidation and simultaneously reducing fatty acid synthesis [13]. ACCs have been used as novel targets for the control of metabolic disorders such as infectious diseases, obesity, and metabolic syndromes [14,15].

Moreover, global diseases like obesity and related metabolic disorders such as dyslipidemia and type 2 diabetes mellitus (T2MD) [16] still need improved targeted therapies. Whereas ACC is the key enzyme for the formation of malonyl coenzyme A (CoA) and has an important role in the regulation of fatty acid biosynthesis and oxidation in humans and other organisms [11,17]. Mammals have two isoforms of ACC identified as ACC1 and ACC2. ACC1 belongs to cytosolic enzymes and is mostly expressed in lipogenic tissues with a key role in the regulation of fatty acid biosynthesis. Similarly, ACC2 belongs to mitochondrial enzymes and is predominantly expressed in oxidative tissues related to mitochondrial fatty acid oxidation [16]. ACC is also an attractive drug target to control both fatty acid oxidation and long-chain fatty acid biosynthesis [18]. Antibiotics that target ACC are not commercially available. A recent study found that inhibiting ACC1 and ACC2 with PP-7a reduce malonyl-CoA levels, fat formation, and weight gain caused by the high-fat diet in the mouse model [19], however, the possible mechanisms underlying PP7a′s pharmacological effects needs further investigation. The ATP binding site of most bacterial biotin carboxylases are structurally similar to the active regions of eukaryotic kinases [20]. Most of the BC inhibitors target the ATP binding site and often stop BC domain dimer formation. Aminooxazole, a well-known BC inhibitor binds to the ATP binding site, although with a lower inhibition constant for CT than BC [21]. SABA1 (Ethyl 4-[2-chloro-5-(phenyl carbamoyl) phenyl] sulfonylamino] benzoate (SABA1) is recently reported to possess antibacterial activity against *Pseudomonas aeruginosa* and *Escherichia coli*. SABA1 might be unique in its function. Unlike other BC inhibitors, SABA1 binds to the biotin-binding site in the presence of ADP [22].

Several studies also suggest the CT domain as a determinant of substrate specificity for biotin-dependent carboxylase complexes [4]. It is confirmed from a conditional mutant of *S. coelicolor* that AccB is important for its viability [23]. The *sace- 4237* gene encodes a putative multidomain ACC in *S. erythraea*, making it the first prokaryotic ACC homodimeric multidomain complex discovered. Both AccB and PccB activity can be performed by SACE 4237 complex and a conditional mutant of *sace- 4237* revealed that *sace- 4237* is required for *S. erythraea* survival [24]. The discovery of multidomain ACCs suggests that domain fusion happened in bacteria during the evolution of these enzyme complexes from single domain subunits to multidomain eukaryotic ACCs.Since AccB contributes to the essential pathway of providing malonyl-CoA, which produces many pharmaceutically important polyketides made by streptomyces [25]. There is a substantial curiosity to understand the pathway(s) which lead to its biosynthesis. The current study aims to determine the crystallographic structure of ACC (AccB) CT domain from *Streptomyces antibioticus* and demonstrate the binding of acetyl-CoA and propionyl-CoA at the binding sites and demonstrate the role of essential residues in the catalytic processing of acetyl-CoA using molecular modelling and biomolecular simulation approaches. Considering the diverse roles of ACC catalyzed product malonyl-CoA, the crystal structure of β subunit of ACC (AccB) from *Streptomyces antibioticus* with a resolution of 2.34 Å has been resolved. The two-step reaction mechanism involving biotin carboxylase (α subunit) and carboxyl transferase (β subunit) has also been highlighted. Moreover, structural biology and biophysical approaches have been deployed to reveal the binding patterns of acetyl-CoA with CT domain. Furthermore, the molecular basis of ACCs substrate specificity is only known for a few species. Therefore, the presented structural data helps to unveil potential key interacting residues for substrate recognition. It will also help to re-design ACCs active site for proficient substrate specificity and produce diverse polyketides. The study will also help in designing novel structure-based inhibitors with potential relevance to obesity and related metabolic diseases.

2. Methodology

2.1. Growth conditions, protein expression and purification

The fragment encoding AccB was amplified from genomic DNA of *S. antibioticus* by using the primers (5′-ATCGTAATCCATATGAGGAAA-CAGCTTGACGAGCTGCTC-3′) containing *Nde*I site (underlined) and (3′TGATTCGATGAATTCTCACTGGGGCGGGTTG CCGTGCTTG-5′) *Eco*RI site (Underlined), and cloned into pET28a. *E. coli* strain DH10B was used for routine subcloning and transformed according to Ref. [26]. Transformants were selected on media supplemented with appropriate antibiotics: 50 mg/ml kanamycin. Plasmid containing *OvmG* gene was transformed into *E. coli* BL21 (DE3). *E. coli* strain BL21 λ (DE3) is lysogenized with λ DE3, a prophage that expresses the T7 RNA polymerase from the IPTG-inducible *lac*UV5 promoter [1]. Rosetta λ (DE3) expresses rare tRNAs to affluence expression of genes that encode rare *E. coli* codons. The transformed cells were grown at 37 °C in shake flasks in Luria Bertani medium supplemented with corresponding antibiotics. Cells were induced with 0.2 mM isopropyl β-D-1-thiogalactopyranoside when grown to an OD_{600} of 0.4 and induction was allowed to proceed for 12 h at 16 °C. Cells were harvested by centrifugation, washed, and resuspended in lysis buffer A (50 mM Tris-HCl, pH 7.5 and 500 mM NaCl). After cells disruption by sonication on ice, debris was separated from the supernatant by centrifugation at 15000*g* for 36 min at 4 °C. The supernatant was passed from Nickel-NTA agarose affinity column (Qiagen), equilibrated with buffer A, followed by subsequent washing with lysis buffer containing 15 mM imidazole (pH 7.5). His-tagged proteins were eluted with a binding buffer containing 300 mM imidazole and purified with Superdex 200 gel filtration column equilibrated with 10 mM Tris (pH 7.5) and 150 mM NaCl. To reduce salt concentration, proteins were exchanged with a buffer comprising of 25 mM NaCl, 10 mM Tris (pH 7.5), 1 mM DTT (pH 7.5). Proteins were concentrated to 12 mg/ml by ultrafiltration through a PM-3 membrane (Amicon) and stored at −80 °C prior to crystallization. Another gene encoding ACCα (containing BC and BCCP domains) was amplified from the genomic DNA of *S. antibioticus* using the primers (5′-

TCGTAATCCA-
TATGAGTCTGCGCAAGGTGCTCATCGCCAACCGTGGC-
GAAATCGCTGTCCGC -3′) containing *Nde*I site (underlined) and (3′TGATTCGATGAATTCTCAGTCCGTGATCTCGCAGATGGCGGCGCCG-
GAGGTGAGGGA -5′) containing *Eco*RI site (Underlined). It was followed by cloning, protein expression, and purification as previously described.

2.2. Crystallization and structure determination

Crystals of AccB were grown in sitting drops by the vapor diffusion method. Drops were generated by adding 2 μl of protein solution and 1 μl of a buffer from a well-containing 500 μl of 1 M lithium sulfate and 0.1 M Bis-Tris (pH 7.5). The subsequent crystals were frozen in liquid nitrogen after soaking for 10 s in a crystallization solution containing 20% (v/v) glycerol. Data was collected at Shanghai Synchrotron Radiation Facility beamlines BL17U and BL18U, and processed with HKL3000. The wild-type crystals belong to the space group $p2_12_12_1$ and the unit cell parameters are a = 117.001, b = 202.390, and c = 204.954. The crystal cell dimensions and space groups are listed in Table 1. Phaser was used for molecular replacement, and the PDB entry 1XNV [3] was used as a search model. The model was built in coot and refined with refmac5 to a final $R_{working}$ of 0.22 and R_{free} of 0.24.

2.3. Enzymatic assay

In vitro activity of AccA and AccB was measured by optimizing the method with different conditions. The reaction mixture contained 50 mM HEPES (pH 7.0), 3 mM ATP, 5 mM $MgCl_2$, 5 mM $NaHCO_3$, 5 mM biotin, 0.5 mM–1 mM acetyl CoA, 20 μM of the purified AccA subunit and 20 μM of the purified AccB subunit in a total reaction mixture of 100 μl. A Control reaction contained all the other stuff except AccA and AccB enzymes. The reaction was initiated by the addition of HEPES buffer, biotin, AccA and kept for 4 h at 30 °C. $MgCl_2$, ATP, $NaHCO_3$, and acetyl-CoA were added to the reaction and kept at 30 °C for another 4 h. After 4 h of incubation, AccB was added and kept overnight at 20 °C. The reaction was stopped with 200 μl MeOH and centrifuged at 12000 g for 10 min, and 25 μl of each was used for HPLC analysis. The supernatant was transferred to a fresh 1.5 ml microfuge tube. The product, malonyl-CoA, was analyzed through HPLC following the available method [27]. A linear gradient from 0.1% TFA in water (buffer A) to 0.1% TFA in MeOH (buffer B) was developed using the following protocol. 0–20 min, 10–90% B; 20–23 min, 100% B; 23–25 min 10% B. The flow rate was 0.8 ml/min, and the absorbance was monitored at 254 nm using DIKMA 5 μM C18 column (250 × 4.6 mm). The same samples were also analyzed through LC-MS by subjecting to negative-ESI LC-MS on Agilent QTOF MS connected to a UV–vis diode array detector with a DIKMA C18, 250 × 4.6 mm, and 5 μm particle size column. For the mobile phase, a linear gradient was developed from water containing 0.1% formic acid (pH 7.0) (solvent A) to 99.9% methanol containing 0.1% formic acid (solvent B), using the following protocol. 0–40 min, 10–90% B; 40–46 min, 100% B; 46–50 min, 10% B at 0.4 ml/min flow rate with detection at 254 nm.

Table 1
Data collection and Refinement Statistics (molecular replacement).

Data Collection	
Space group	$P2_12_12_1$
a, *b*, *c* (Å)	117.001, 202.390, 204.954
Resolution (Å)	39.74–2.34
R_{merge}	0.105 (0.530)
I/σ (*I*)	13 (2.3)
Completeness (%)	99.1 (94.6)
Redundancy	6.4 (5.9)
Refinement statistic	
Resolution (Å)	50–2.34
Unique reflections	192724
$R_{working}/R_{free}$	0.22/0.24
No. of atoms	
Protein	23450
Water	99
SO_4	30
GOL	24
B-factors	
Protein	44
Water	32
SO_4	59
GOL	50
RMSD	
Bond lengths (Å)	0.005
Bond Angles (°)	1.351
Ramachandran Plot (%)	
Favored	95.83%
Allowed	3.29%
Outliers	0.88%

2.4. Molecular docking and in silico mutagenesis

To grasp the binding of the acetyl-CoA substrate with the binding site of AccB and determine the key residues required for the substrate processing, molecular docking using Auto Dock Vina, blind docking protocol, was performed [28]. The structure of Acetyl-CoA was retrieved from the PubChem database using accession ID: CID444493. The structure was prepared and minimized prior to molecular docking. The Post-docking complex of AccB and acetyl-CoA substrate was subjected to structural mutants modeling known as alanine scanning, which is a site-directed mutagenesis approach and determines the impact of alanine substitution on the binding of the small.

Molecule or protein-protein complex. Alanine is a preferable choice because of its inert nature, non-bulky with methyl functional group, and can adopt the secondary structure of any other amino acid. This *in silico* alanine substation method is also very useful in determining the biological importance of particular residue in the inhibitor or substrate binding [29–32]. For structural mutants mCSM–lig tools [33,34] were used to substitute the interacting residues with alanine. mCSM–lig, a structure-guided *in silico* approach quantify the effects of mutations on affinities of small molecules or substrates for proteins. mCSM-lig uses graph-based signatures to train a predictive model using a representative set of protein-ligand complexes, which have shown a strong correlation with the experimental data. The protocol of *in silico* mutagenesis used in this study has been explained in the previous study [35]. In order to determine the binding specificity of AccB for propionyl-CoA, we performed docking of propionyl-CoA for which the experimentally reported residues in other species are already defined. The structure of propionyl-CoA was retrieved from the PubChem database using accession ID: CID92753 and processed as previously discussed.

2.5. Molecular dynamics (MD) simulation

The wild type and mutant type complex were subjected to molecular dynamics (MD) simulation studies using the AMBER20 package [36]. The TIP3P water model was used, and the system was neutralized by Na^+ counter ions addition. The system was energy minimized by using the steepest descent algorithm. Restraining simulation of the position was employed to equilibrate the system and solvent around the protein before the actual simulation. In a constant number of atoms, volume, pressure, and temperature (NPT and NVT), ensembles were applied to the system for the MD simulation studies. Particle Mesh Ewald (PME) SHAKE algorithm was used for hydrogen interactions [37]. A total of 100ns of MD simulations for each system was performed. CPPTRAJ and PYTRAJ [38] was used for RMSD, RMSF, and other analysis of the MD trajectories. PyMOL was used for visualization [39]. Furthermore, we also calculated the total energies of all the systems, including wild type and mutants.

2.6. Binding free energy calculations

The MM/GBSA method was used to calculate the free energy of binding between WT and MTs complexes [40]. A total of 5000 conformations extracted from the 100ns trajectories of 0.2 ns time intervals were used in the calculation. Molecular Mechanics/Generalized Born Surface Area (MM/GBSA) is an efficient approach to analyze free energy. The values of MM/PBSA are significantly in correlation with experimental approaches [41]. This method has been used by a large number of studies to estimate the binding free energy for various biological complexes. Here, we MM/GBSA approach to calculate the binding free energy.

For Free Energy calculation, the following equation was used:

$$\Delta G(\text{bind}) = \Delta G(\text{complex}) - [\Delta G(\text{receptor}) + \Delta G(\text{ligand})]$$

Each component of the total free energy was estimated using the following equation:

$$G = G_{bond} + G_{ele} + G_{vdW} + G_{pol} + G_{npol}$$

Where G_{bond}, G_{ele}, and G_{vdW} denote bonded, electrostatic, and van der Waals interactions, respectively. G_{pol} and G_{npol} are polar and nonpolar solvated free energies. The G_{pol} and G_{npol} are calculated by the generalized Born (GB) implicit solvent method with the solvent-accessible surface area SASA term.

3. Results and discussion

Previously, several biotin-dependent carboxyl transferase structures have been determined, including glutaconyl-CoA decarboxylase (for sodium-ion pump) [42], yeast-CT (for acetyl- CoA carboxylation) [43], PCC form *S. coelicolor* (for propionyl–CoA carboxylation) [3], AccD5 from *M. tuberculosis* (for propionyl- CoA carboxylation) [44] and transcarboxylase 12S (for pyruvate carboxylation) [45]. The crystal structure specifies that, unlike the yeast carboxyltransferase dimeric CT domain, AccB is a 340 kDa homohexamer, comparable to 12S (a methylmalonyl-CoA transcarboxylase) from *Propionibacterium shermanii*, AccD5 from *M. tuberculosis*, and PccB (CT domain) from *S. coelicolor* [3,7,46] The active site of all these crystal structures are suggested to be positioned at the dimeric interface except for methylmalonyl-CoA (MMCoA) decarboxylase [47]. Herein, the crystal structure of AccB (CT) from *S. antibioticus* has been explored. *S. antibioticus* (Strain ATCC11891) mainly produces two macrolide antibiotics, oleandomycin, and oviedomycin. Specifically, the products of *OvmH* and *OvmG* genes from *S. antibioticus* are related to polyketide metabolism. They are not usually found in the biosynthetic gene clusters but present elsewhere in the chromosome and contribute to the primary metabolism functions [48]. These two genes are very similar to α and β chains of the acetyl-CoA carboxylase complex. In turn, the enzyme complex provides malonyl-, propionyl- and butyryl-CoA to regulate the first committed step in the biosynthesis of polyketides and fatty acids [48]. These gene products are also involved in the metabolism of fatty acids. The α chain (OvmH) contains biotin carboxylase at the amino (N) terminus, which incorporates CO_2 into the biotin residue attached to BCCP (biotin carboxylase carrier protein) at the carboxy (C) terminus. Similarly, the didomain mediated dimeric interaction is highly conserved among biotin-dependent carboxylases and is vital for enzyme stability, catalysis, and substrate specificity [3]. On the other hand, the β chain (OvmG) is related to carboxyl transferase activity which deliver malonyl-, ethylmalonyl, or methylmalonyl- CoA through trans--carboxylation of biotin-CO_2 to acetyl-CoA, propionyl-CoA, and butyryl-CoA. ACC in *S. antibioticus* is a multi-subunit complex. The catalytic beta subunit of ACC is a 340 KD homo-hexamer responsible for catalyzing *trans*-carboxylation between biotin and different acyl-CoA substrates. In this study, the crystal structure of β subunit of ACC (AccB) from *S. antibioticus* with a resolution of 2.34 Å was resolved. The ACC crystal structure was then subjected to advanced computational methods for further analysis. Our results revealed the three key residues work in triangle coordination where the two tails of the substrate are fixed by two glutamine residues (Gln 346, Gln 514), while the backbone of the substrate is fixed by Val223 residue.

In order to confirm the conservancy of the key interacting residues (V223, Q346, Q514) with acetyl- CoA, sequence alignment of *S. antibioticus* AccB was performed with the different species including *M. tuberculosis, S. coelicolor*, *S. erythreus, S. cerevisiae*, and *human* (Supplementary Fig. S5). The alignment indicated that V223 is conserved across the species Corresponding to V247 in *M. tuberculosis*, V236 in *S. coelicolor*, V229 in *S. cerevisiae*, V258 in S. erythreus, and V245 in humans. However, Q346 and Q 514 are partially conserved across the species which might be the reason that these ACCs use Propionyl-CoA as a preferred substrate as an alternative to acetyl-CoA. Q346 of AccB corresponds to Q348 in S. *cerevisiae, Q348* in *S.*erythreus, and Q364 in humans, while this position is occupied by arginine residue in *S coelicolor* and *M. tuberculosis*. Q 514 is also partially conserved across the species and is correspond to Q527 in *M.tuberculosis*, Q529 in *humans,* and Q481 in *S. cerevisiae*. These residues are not previously reported for ACC binding. Our results demonstrate that these key interacting residues are important for substrate binding and stability, particularly acetyl-CoA, and may be considered for mutations to acquire the substrate specificity for new products of natural "un-natural" origin. For instance, the binding of propionyl- CoA share stronger conservancy and alignment of the key residues such as the two consecutive glycine residues for catalytic binding of the substrate provide enough evidence for almost the same mechanism of catalysis by different species.

The novel crystal structure of AccB from *S. antibioticus* is reported in this study. Moreover, the interacting residues involved in the formation of AccB- substrates (acetyl-CoA and propionyl-CoA) complexes were also explored. In addition, the structure and sequence of AccB were also compared with the previously identified structures, which revealed a higher sequence and structure homology with PccB of *S. coelicolor* and AccD5 of *M. tuberculosis*. Interestingly, based on the structural homology only the propionyl binding residues were found to be similar across the three species. However, the AccB was crystallized with a good resolution and further computational approaches were applied to depict the potential interactions of AccB with acetyl-CoA and propionyl-CoA. Still, further Co-crystallization studies are required which includes obtaining the crystal structure of AccB in Complex with acetyl -CoA and Propionyl CoA. Such analyses may further clarify the interactions of AccB with its natural substrates explored in this study.

3.1. Overall fold

Crystal structure of the apo ~340 KD wild type AccB hexamer was determined and refined to a resolution of 2.34 Å. The structure has a ring-shaped architecture and overall dimensions of 117.001 Å × 202.390 Å × 204.954 Å, While the internal pore size ranges from 10 to 20 Å (Fig. 1B). The CT domain of *S. antibioticus* shared a sequence identity of about 57%, 56%, 52%, and 51% with the previously reported ACCs from *S. coelicolor*, *Saccharopolyspora erythraea, Mycobacterium tuberculosis,* and transcarboxylase 12S structure, respectively. The AccB structure was also superimposed for comparative analysis with previously reported structures including *M. tuberculosis*, transcarboxylase *12S, S. coelicolor, E. coli*, *Human, and S. cerevisiae,* which yield root-mean-square deviation values of 0.60 Å, 0.71 Å, 0.62 Å, 1.23 Å, 1.69 Å and 1.84 Å respectively (Fig. S3). Similar to the *S. Coelicolor* PccB used for molecular replacement [3], the AccB hexamer has a 32-fold symmetry, where a 2-fold axis is perpendicular to a 3-fold axis (Fig. 1B). The overall structure closely resembles the reported ACC structures and hexamer assembly followed the ring-shaped complex architecture. Like PccB, yeast CT and 12S [3,43,45], the resulting crystal structure is composed of two subdomains: NTD (N-terminal domain) (1–257), and CTD (C-terminal domain) (261–514). Subdomain NTD contains 5

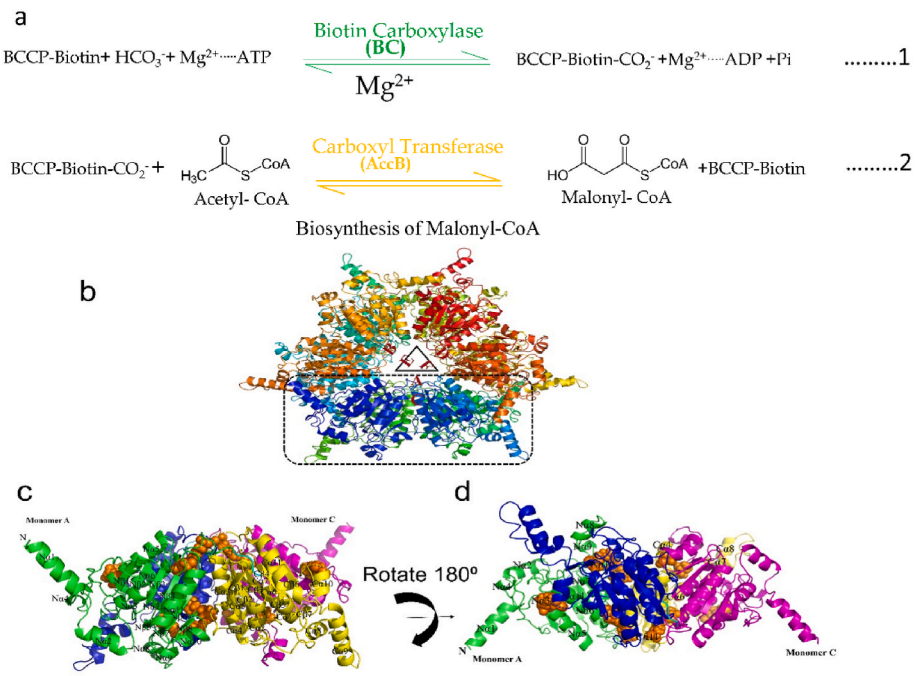

Fig. 1. (A) Two-step reaction of ACCs. (B) Overall hexametric structure of ACCβ. The hexamer has 32-fold symmetry; especially it forms two stacks of three monomers (A-B-C and D-E-F) related by a 3-fold axis (indicated by triangle), while A-C, B-E, and D-F monomers form three tightly interacting dimers related by the 2-fold axis shown in panel C. Monomer A of ACCβ, colored from N- terminus (green) to C terminus (yellow) with two structurally similar domains (N and C). Monomer C is shown in magenta and blue under monomer A. (D) Monomer A and C are in the same colors after a 90° rotation. Interaction between the two monomers is shown as spheres (orange). The helices of N-domain (Nα10, Nα11) of monomer A interact with the corresponding helices of the C-domain (Cα3, Cα4, Cα5) of monomer C.

parallel β sheets (β1 74–78, β2 87–91, β3 122–126, β4 159–163, β5 166–168) and 1 antiparallel β sheet (β6 180–184) on one side and 2 parallel β sheets (β7 189–191, β8 226–228) on another side of the amino (N) terminus. Similarly, subdomain B contains 4 parallel β sheets (β1 307–314, β2 317–324, β3 355–359, β4 393–397) and 1 antiparallel (β5 400–402) on one side and 2 smaller parallel β sheets (β6 418–421, β7 426–428) on another side of the Carboxy (C) terminus. The β sheets in subdomain NTD and subdomain CTD are flanked by 11α helices each, respectively (Fig. 1C). The interaction between trimers (A-B-C to D-E-F), along with the six active sites are located at the dimer interface of one monomer N- domain (Nα10, Nα11) with its dimeric partner C-domain (Cα3, Cα4, Cα5), (Fig. 1C and D). From our structure, the intertrimer interaction (A-C, B-E, D-F) is in contrast with the previously reported (A-D, B-E, C–F) [3,43] and include E102 (OE1−NH_2)-R474, T151 (O═NH1)- R507, S154 (O═NH1)-R507, I192 (N−OE2))-E371, S221 (O═NE)-R377. However, the dimer interactions are highly conserved between AccB, PccB, and AccD5, which highlight the importance of coordination between monomers for efficient substrate binding and stability. Significantly, AccB, PccB, and AccD5 follow a similar reaction mechanism, whereas, AccD4 and AccD6 have different oligomeric architecture, and may be different from the hexameric ring structure of AccB, PccB, AccD5, and 12S [44]. Moreover, intertrimer interaction mainly occurs between the N-terminal helices of one monomer and C terminal helices of its dimeric partner (Fig. 1C and D). The overall structure demonstrates the reputation of interdomain interaction for stability, flexibility, and activity of biotin-dependent carboxyl transferases, such as AccB, PccB, 12S, AccD5, and yeasts-CT.

3.2. Enzymatic assay

AccA and AccB *in vitro* activity was measured by optimizing the HPLC method with different conditions. The expected peaks were observed at the retention time of 8.49 min, and 10.55 min, which were in accordance with our standard malonyl-CoA, and acetyl-CoA respectively [27]. The same samples were also analyzed through LC-MS/MS. We observed a major peak for the corresponding product (malonyl-CoA) at 852.1057 (expected 852.1083) (Supplementary Figs. S1 and S2).

3.3. Molecular docking and alanine scanning results

The binding mode of acetyl-CoA was revealed through molecular docking simulation which predicted that substrate is tightly bound between the N Domain (Nα6) of one domain and (Cα6) of the other corresponding C domain (Fig. 2A). The best binding conformation possesses the docking score of −8.59 kcal/mol. The substrate interacts with AccB by forming three hydrophobic interactions, six hydrogen bonds, and two salt bridges. Among the hydrophobic interactions Ala176, Val286 and Lys381 are involved in direct interaction with the substrate. Furthermore, the only two salt-bridges interactions are formed by His225 residue with the substrate. Moreover, the.

Key hydrogen interactions are important for the recognition of the processing of the substrate. Herein, six hydrogen bonds were established by Asp179, Val223, Ser343, Gln346, Ser350, and Gln514 residues with the acetyl-CoA. The 3D bonding pattern of acetyl-CoA with the AccB is shown in Fig. 2b while the 2D interactions are shown in Fig. 2c. Moreover, acetyl-CoA is attached in the active site of the CT domain at the CT dimer interface between the two monomers, which is highly enriched with electronegative amino acids (Fig. 2d). These findings are consistent with the previous reports on the same protein from different species, which reported that the binding cavity is occupied by strong electronegatively charged amino acids [6]. To understand the role of each of the binding site residues involved in interaction with the substrate, we performed alanine scanning. Alanine scanning is experimentally and computationally the most reliable approach to determine the impact of alanine substitution on the binding of substrate and protein stability. It has been previously used to explore the key binding residues, which is important for different biological processes, i.e., RNA/DNA recognition, enhanced catalysis, improved substrate recognition, and identification of key hotspots critical for disease induction. Considering the importance of this approach here, we also employed alanine scanning to understand the role of each interacting residue with acetyl-CoA. Using mCSM-lig [49], it was observed that among the total seven residues, only three residues V223, Q346, and Q514 reduced the affinity by manifold while the other residues didn't affect the binding substantially. Upon the alanine substitution at position V223 the binding affinity changed by −3.21 kcal/mol. The substitutions at positions Q346 and Q514 significantly reduced the binding affinity by −2.98 kcal/mol and

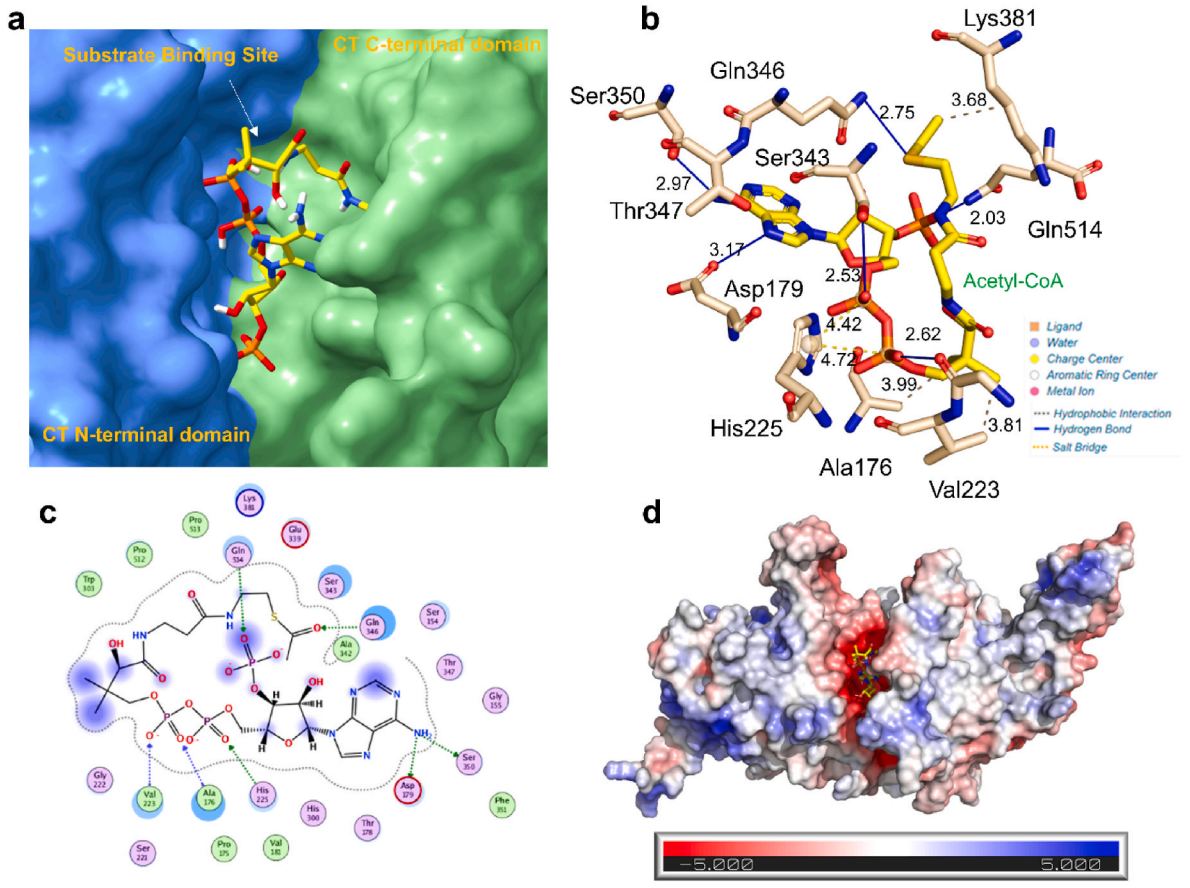

Fig. 2. (A) Molecular surface of the binding site for acetyl CoA in the *S. antibioticus* CT domain. The N domain of one monomer is colored in blue and the C domain of the other monomer in green. PyMol visualization software was used for the surface representation of the complex. (B) Substrate 3D interactions pattern of key amino acids in the substrate-binding cavity. The specific interaction labels are given in the panel b figure legend. The hydrogen bonds lengths are given in angstrom (Å) (C) represent the 2D interaction pattern of the acetyl-CoA with the substrate-binding site residues (D) Electrostatic potential surfaces of ACCB. Surfaces are colored from red (−5 keV) to blue (5 keV). The substrate-bound in the pocket is enriched with electronegative amino acids. The N domain of one monomer is colored in cyan and the C domain of the other monomer in green. The overall structure exhibit more electronegative amino acids.

−3.05 kcal/mol. The importance of these residues was further established by visual analysis, which shows that these three residues help in the fixation of the substrate. The two tails of the substrate are fixed by Gln346 and Gln514, while the backbone of the main scaffold is fixed by Val223. The two residues Val223 and Gln514, residues in a loop region, while the Gln346 lies in the strong helix. Consequently, this shows that these three residues may play a significant role in the recognition and catalysis of acetyl-CoA. Hence, to further understand the role of these residues in the catalysis, we subjected these three mutant complexes along with the wild type to all-atoms simulation to explore variations in the dynamics features associated with these substitutions and their impact on the binding affinity. The alanine scanning results predicted by different algorithms are given in Table 2.

Table 2
Predicted affinity change upon the alanine substitution. All the values are given in kcal/mol.

Wild Residue	Position	Mutant Residue	Affinity Change
Asparagine	179	Alanine	−0.71
Glycine	223	Alanine	−3.21
Serine	343	Alanine	−1.05
Glutamine	346	Alanine	−2.98
Threonine	347	Alanine	−1.23
Serine	350	Alanine	−0.95
Glutamine	514	Alanine	−3.05

3.4. Binding and specificity of Propionyl-CoA

In order to determine the binding specificity of AccB for propionyl-CoA, we performed docking of propionyl-CoA for which the experimentally reported residues in other species are already defined. According to previous literature, Gly182 and Gly183 in *S. coelicolor* PccB [3] and Gly193 and Gly194 in *M. tuberculosis* AccD5 [44] hydrogen-bond with the carbonyl group of propionyl-CoA. These ACCs share the highest identity with our structure and are reported to be responsible specifically for the propionyl-CoA binding. These two key adjacent glycine residues are conserved in ACCs and correspond to Gly169 and Gly170 position in our structure. Hence, docking was performed against these residues which revealed a docking score of −7.34 kcal/mol. Our analysis revealed that the binding of propionyl-CoA occupies Gly136, Ala168, Gly170, and Gly194 which strongly align with the previous reports. Interestingly, one among the two important glycine residues, Gly169 and Gly170, the one at position Gly170 establishes a stronger hydrogen bond with propionyl-CoA, thus showing the specific binding at this site. The binding pattern of propionyl-CoA is shown in Supplementary Fig. S4. The partially conserved residues Q472, R471, and F468 of AccD5, which are responsible to interact with the bisphosphate group, correspond to Q514, R441, and V438 in AccB. The specific interaction pattern and effect of Q514 are discussed in detail (refer to 3.4 and 3.5). Our findings validate the previously reported pattern of the key binding residues and location of the active site for ACCs which use propionyl-CoA as a substrate.

3.5. Dynamic features and underlying mechanism of substrate binding and processing

Structural-dynamics behavior of the wild type and mutant complexes were estimated to decipher the stability, flexibility, and compactness of each complex. For stability assessment, RMSD as a function of time was computed for the wild type and presented in Fig. 3. The wild-type complex assessment revealed that the structure exhibited more stable behavior than the mutants. The RMSD of the wild type increased initially and attained the equilibrium soon after reaching 10 ns The structure stabilized at 3.0 Å. Acceptable deviation at different time intervals during the first 20ns was observed; however, the structure did not converge substantially from the mean position during the 100ns simulation time. For instance, major deviations were observed at 20 ns, 25 ns, and 38ns while the structure then remained stable for the rest of the simulation time. To thoroughly investigate the variations at these particular time points, we extracted structural frames and studied further to understand the molecular mechanism of substrate binding and the impact of alanine substitution on the binding and stability of the protein. In the wild type, at 20 ns particularly the loop between 501 and 514 deviation is less than the native structure, and this can be witnessed from Fig. 3C. On the other hand, at 25ns it was observed that the increment in RMSD is associated with the opening of the loop, which helps the substrate to move inward and outward from the binding cavity Fig. 3D. As witnessed in the native structure with closed-loop, the substrate occupied the cavity, while at 25ns the loop is displaced significantly, which eventually moves out of the substrate from the cavity. At 38ns the RMSD was also maximum. Extraction of structure coordinates at 38ns revealed a greater deviation of the loop and substrate from its mean position, thus causing more RMSD variations. Afterward, the RMSD decreased substantially, thus passing the substrate inside the binding cavity and causing stabilized binding. In the average structure, the substrate and loop are relocated in the nearly original position, showing that substrate binding is stabilized except at the aforementioned time intervals. The three residues important for substrate binding shows that it works in triangle coordination where the two tails of the substrate are fixed by two glutamine residues (Gln 346, Gln 514), while the backbone of the substrate is fixed by Val223 residue. On the other hand, the V223A structure exhibits significant structural deviation. From the start of simulation, the RMSD increased continuously and reached 4.0 Å in the first 20 ns This trend gradually increased over time but the RMSD remained lower between 20 and 40ns. Afterward, the RMSD increased gradually again and the substantial structural deviation was observed until 100 ns The variation observed in Fig. 4A were mapped onto their respective structures and explored the binding mechanism. In the case of V223A, significant variations were observed at 20 ns, 40 ns, 44 ns, 58 ns, 72 ns, 78 ns, and 80ns time intervals. At 20 and 40ns decreased RMSD value was recorded. Investigations of the structural coordinates at these particular time points revealed less deviation of the loop residue (500–514) and also the loop residue Val223, which is the probable reason for less deviation of RMSD. On the other hand, increment in the RMSD value is associated with the significant movement of the loop (500–514) and the loop exhibiting residue V223 moved away from the substrate. Thus, opening the cavity which helps the substrate to evade out of the binding cavity.

Furthermore, the observation, such as movement of the loop having residue Val223 destabilizes interaction with the substrate, thus affecting the backbone fixation of Acetyl-CoA. The structural coordinates are presented in Fig. 4B, C, and 4D. Correspondingly, the Q346A displayed a little unstable behavior during the first 50 ns, however then gained stability and remained stable for the last 50 ns In the initial 50ns simulation of Q346A, the RMSD increased to 3.0 Å, and significant structural perturbation was recorded. Furthermore, the Q514A faced significant structural deviation and remained unstable during the 10 ns At 8ns the RMSD abruptly increased and reached 3.5 Å. This pattern was steady until 60 ns, afterward, the RMSD increased in the following simulation time and substantial structural perturbation was seen between 70 and 80ns. During 70–80ns the average RMSD reached 5.0 Å. The RMSD then decreased and remained uniform 100 ns In the case of Q346A, significant fluctuations were observed at 20ns,47 ns, and 48ns time intervals.

Investigations of the structural coordinates at these particular time points revealed more deviation of the loop residue (500–514) and the helix residue prevailing Q346A pushed away, which subsequently

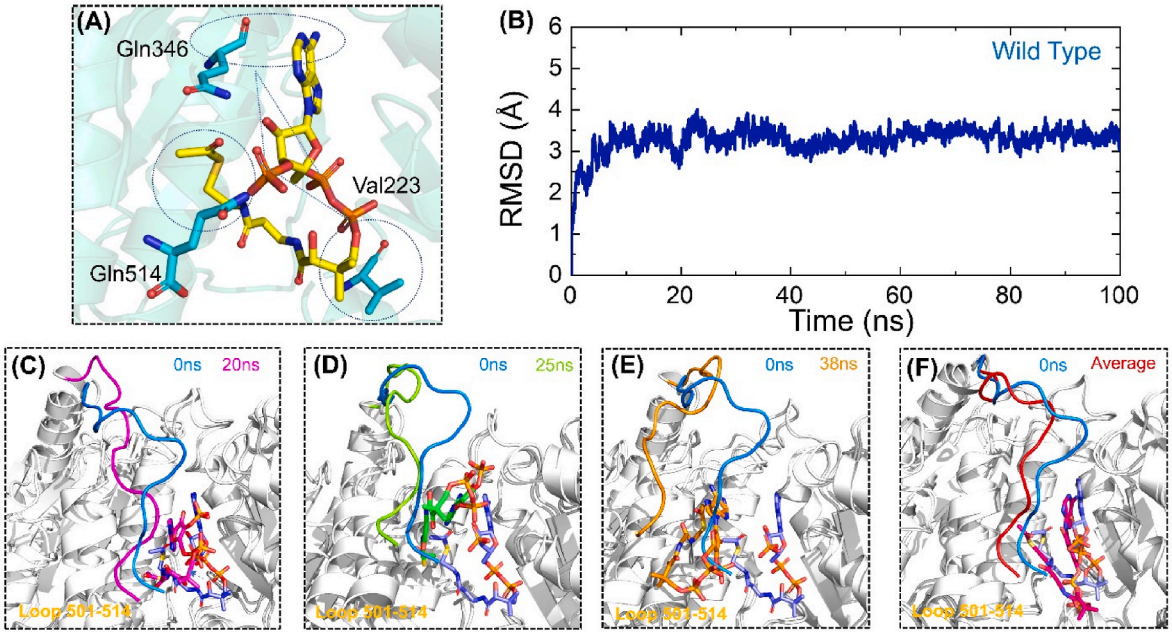

Fig. 3. Representation of the structural stability of the wild type and depiction of the atomic variations associated with the binding and stability. (A) represent the three important residues that help in the fixation of the substrate. (B) display the stability graph as RMSD. (C) (D) (E) and (F) represent the variations captured during the simulation at different time intervals shown in different colors. The substrate binding and the loop 501–514 are shown in different panels at a particular time point.

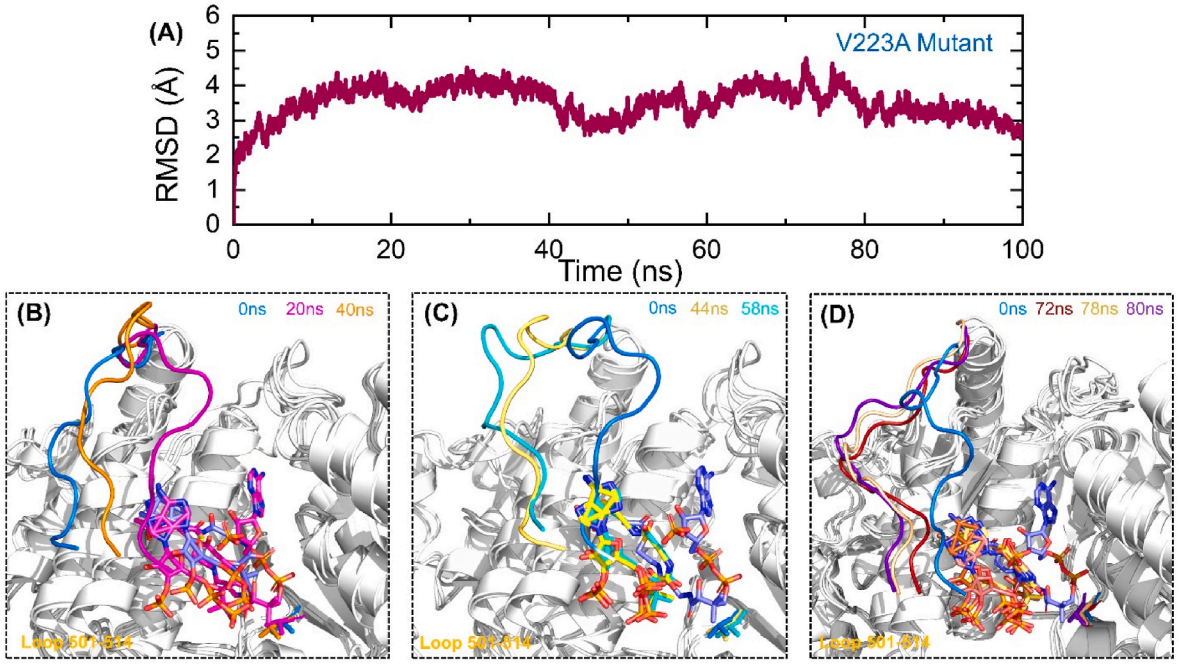

Fig. 4. Representation of the structural stability of the V223A complex and depiction of the atomic variations associated with the binding and stability. (A) display the stability graph as RMSD. (B) (C) and (D) represent the variations captures during the simulation at different time intervals 20 ns, 40 ns, 44 ns, 58 ns, 72 ns, 78 ns, and 80ns are shown in different colors. The substrate binding and the loop 501–514 are shown in different panels at a particular time point.

opened the binding cavity and helped the substrate to escape from the binding cavity Fig. 5C. Moreover, movement of the helix exhibiting residue Q346 destabilizes the substrate interaction and tail fixation of the acetyl-CoA. This shows that the alanine substitution has altered the binding stability of the substrate. This shows that the binding is stabilized by the interactions with these key residues, such as V223, Q346, and Q514. For Q514A mutant higher deviations were observed at specific time intervals of 8 ns, 65 ns, 69 ns, 72 ns, and 83 ns Fig. 5D and E. Higher RMSD is observed at 83 ns, whereas the low RMSD value is observed at 6 nsas compared to the native structure. Q514A destabilizes the substrate binding and tail fixation, which is consistent with the effect of V223A and Q346A.This helps the substate to evade out of the binding cavity.

Furthermore, we also calculated the structural compactness as the radius of gyration *(Rg)*. In case of the wild type the structure initially remained open however, after 10ns the *Rg* value decreased from 27.6 Å to 26.8 Å. This pattern was continued until 100ns and the average *Rg* was reported to be 26.4 Å. Unlike the wild type the three mutants

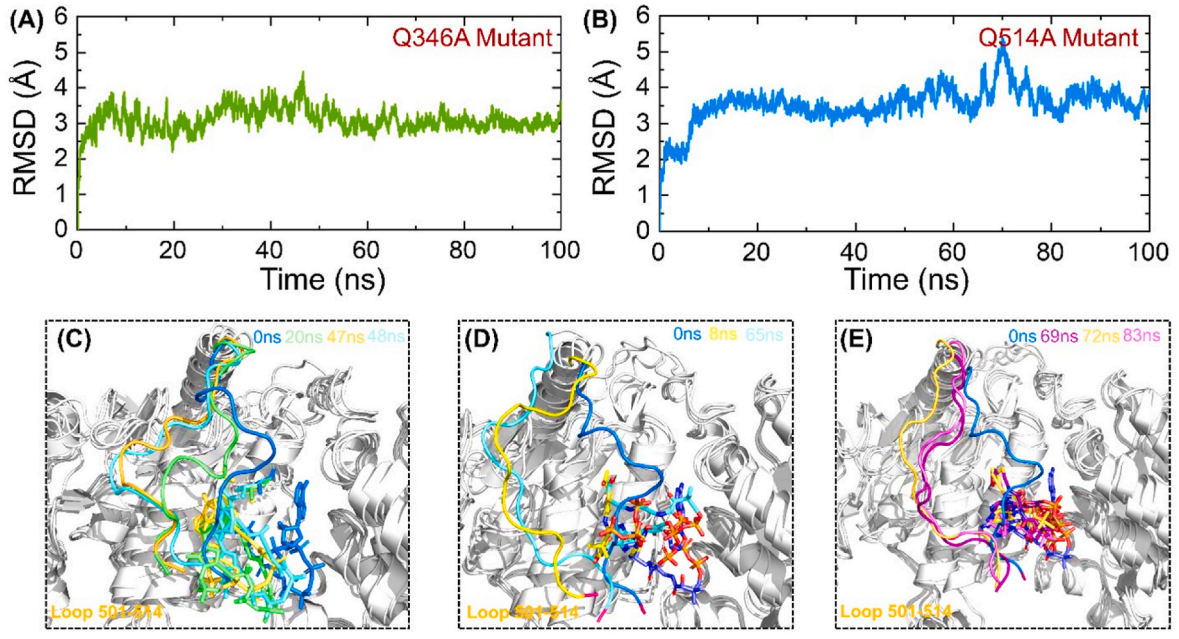

Fig. 5. Representation of the structural stability of the Q346A and Q514A complexes. (A) and (B) display the stability graphs for Q346A and Q514A as RMSD. (C) represent the variations captured during the simulation at different time intervals 20 ns, 47 ns, and 48ns experienced by the Q346A complex. (D) and (E) represented the structural deviations at different type points imposed by the alanine substation in the Q514A mutant complex. Each complex is shown in different colors. The substrate binding and the loop 501–514 are shown in different panels at a particular time point.

V223A, Q346A, and Q514A remained less compact than the wild type. For V223A, the average *Rg* was 27.3 Å, for the Q346A, the average *Rg* was reported to be 27.0 Å while for the Q514A, the average Rg was 27.3 Å. This shows that the mutations have caused the unbinding of the substrate and thus causes the structure to open up the two domains freely and weaken the binding. The *Rg* graphs for each complex are shown in Fig. 6. The x-axis shows the total number of frames, while the y-axis shows *Rg* in Å.

To understand the dynamics–function relationship as a protein motion, RMSFs value of backbone Cα was calculated and compared. The higher RMSF value is an indication of a flexible region with more movements, whereas the low RMSF value suggests a rigid region and shows minimal movements during the simulation. Herein RMSF was calculated to understand the residual flexibility of each complex, including the wild type and mutants. Higher flexible regions were mapped in all the complexes and shown in Fig. 7A. It can be seen in Fig. 7A that all the complexes wild type, V223A, Q346A, and Q514A, exhibit a more similar pattern of minimal residual flexibility except higher flexibility in some regions, i.e., 50–75 (γ1), 187–220(γ2), 250–270(γ3), 360–375(γ4), 420–470(γ5) and 497–514(γ6). This shows that the mutation has epistatically increased the flexibility of the region, which is stabilized by the binding of the substrate in the wild type. Correspondingly, these regions which exhibit higher fluctuation are shown in Fig. 7B and C. These variations in the fluctuation may affect the binding of the substrate and conformational optimization differently in each system. Importantly the loop which acts as an opening and closing switch exhibit higher fluctuation in the holo states, which define its functional significance. The RMSF graphs for each complex are shown in Fig. 7.

To further understand the impact of these substitutions on the total hydrogen bonding changes and binding affinity, we performed hydrogen bonding analysis and free energy calculations using the MM-GBSA approach. The total number of hydrogen bonds in each simulation trajectory of the wild type, V223A, Q346A, and Q514A mutants are shown in Fig. 8. During the 100ns simulation, an average of 251 hydrogen bonds was sustained, while in V223A a total of 248 hydrogen bonds were recorded. On the other hand, the hydrogen bonds count was substantially reduced to 242 in the Q346A mutant while 245 in the Q514A complex. This shows that the wild-type structure favorably binds the substrate and efficient process for the chemical reaction. Correspondingly the hydrogen bonds count reduced in mutant complexes shows that the three residues V223, Q346, and Q514 may play an essential role in the recognition and processing of the substrate. Furthermore, determining the half-life of important hydrogen bonds during the simulation informs important information about the binding and unbinding events and the significance of each residue in the substrate recognition and processing. Thus, to quantify the role of V223, Q346, and Q514 in the binding of acetyl-CoA, we calculated the half-life of these three important residues. Consequently, it was observed that in the wild type the contribution of these three residues was substantial. In the wild type, it was observed that the half-life of the three residues was reported to be 74% (V223), 82%(Q346), and 59% (Q514), respectively. On the other hand, in the V223A complex significant decline in the half-life of hydrogen bonds formed by the V223 was observed. The findings revealed that upon the substitution, the half-life for V223A was reported to be 36% only. For the other residues relatively reduction in the half-life was observed. In the V223A complex, the total half-life of Q346 was 79% and 42% for the Q514 residue was observed. Moreover, estimation of the half-life of the hydrogen bonds for the aforementioned three residues also revealed different quantities in the Q346A complex. In this complex, hydrogen bonds in the simulation trajectories were observed to be sustained for 48% (V223), 43%(Q346), and 51%(Q514), respectively only. The Q514A complex showed a greater decline in the hydrogen bond, particularly for the alanine substitution at Q514. In

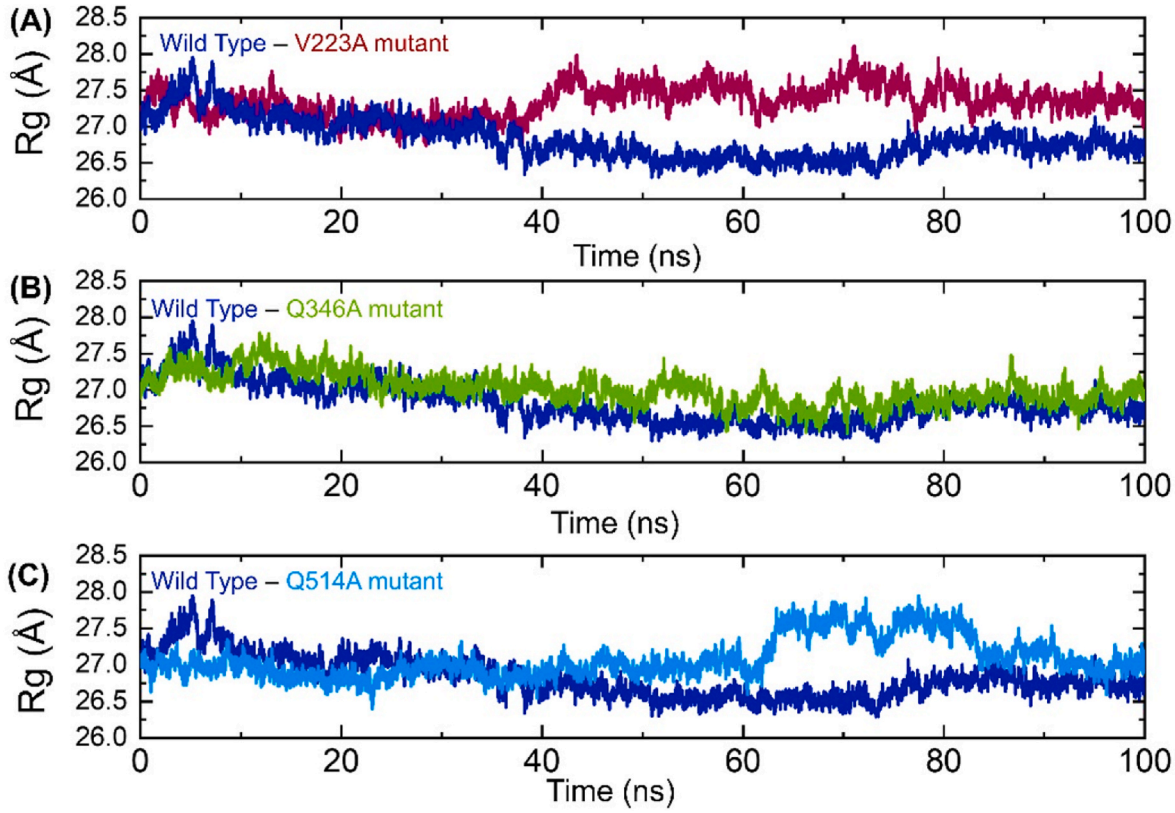

Fig. 6. Show the *Rg* graph of each complex. (A) Represent the comparative Rg of the wild type and V223A mutant complex, (B) represent the comparative Rg of the wild type and Q346A mutant complex while (C) represent the comparative Rg of the wild type and Q514A mutant complex. The x-axis shows the total number of frames while the y-axis shows *Rg* in Å. A 100ns trajectory was used to calculate the compactness as *Rg*.

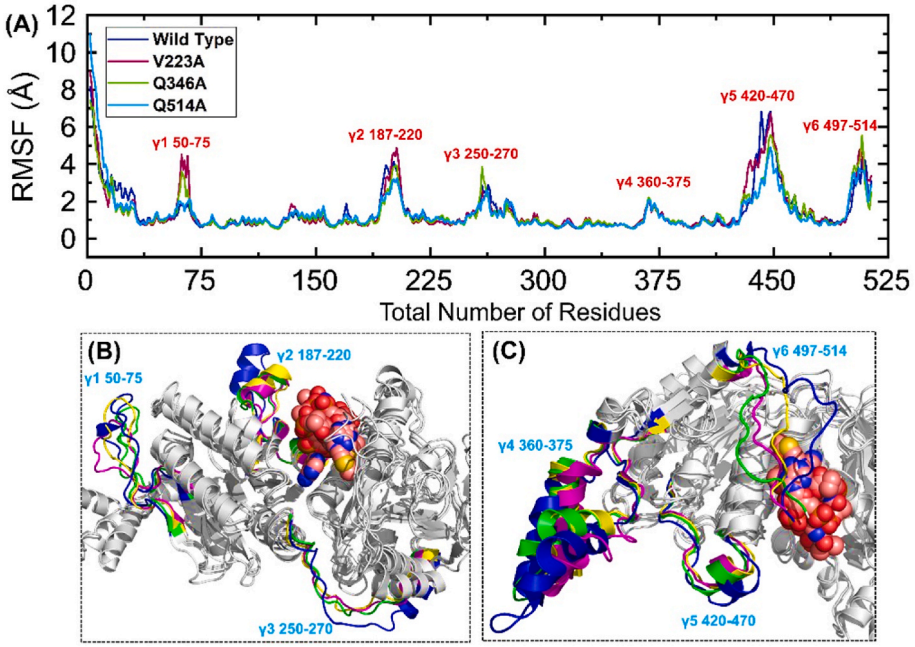

Fig. 7. The RMSF graphs for each complex are shown in different colors. (A) RMSF graph for all the complexes. The graph also shows the six important regions which exhibit higher fluctuation than the others. (B) and (C) represent the higher flexible regions colored and tagged differently. The x-axis shows the total number of residues while the y-axis shows RMSF in Å.

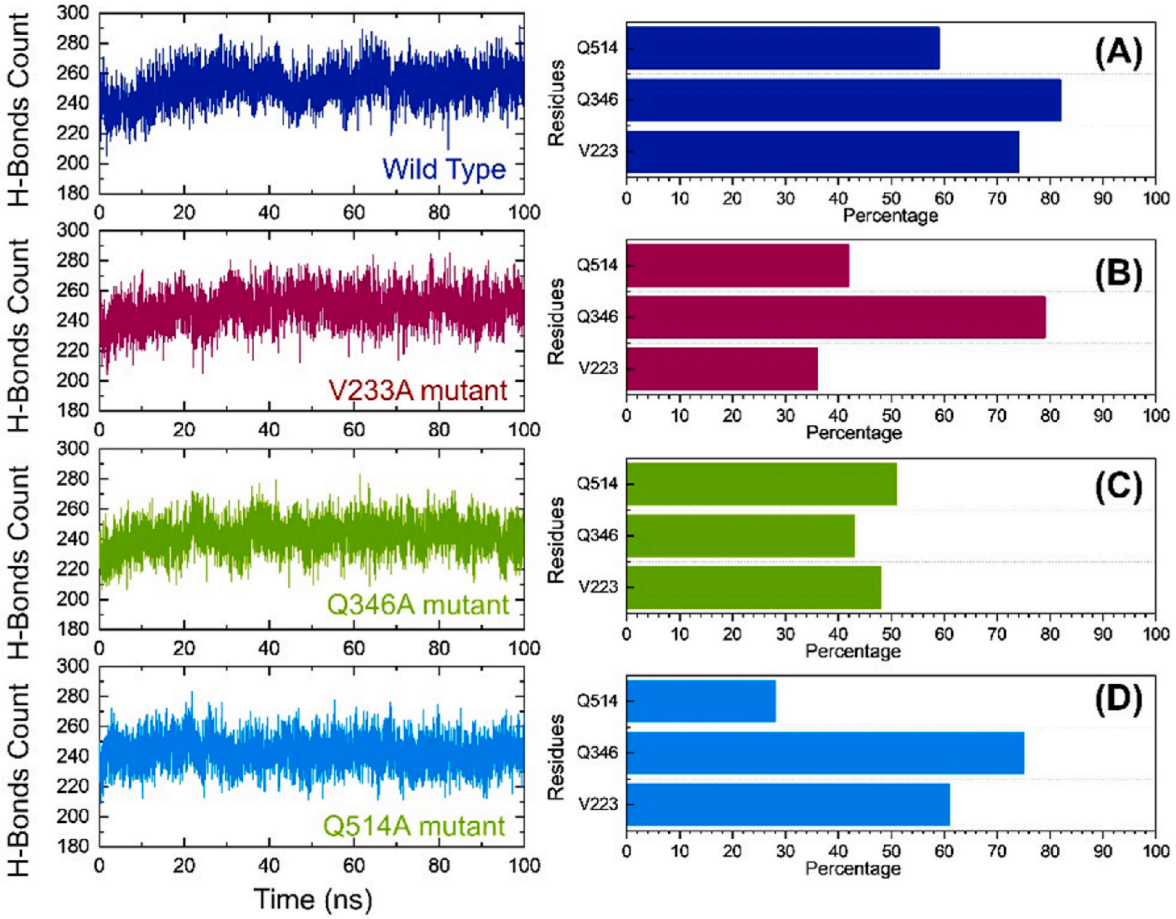

Fig. 8. The H-bond graphs for each complex are shown in different colors. (A) Display the intra and inter hydrogen bonds in the wild type, (B) display the intra and inter hydrogen bonds in the V223A mutant complex, (C) display the intra and inter hydrogen bonds in the Q346A mutant complex, while (D) display the intra and inter hydrogen bonds in the Q514A mutant complex. The x-axis shows the total number of frames while the y-axis shows the H-bonds count.

numbers, the bond formed by Q514A was observed in only 28% structural frames, while the hydrogen bond of the other two residues i.e., V223 and Q346 was reported to be sustained only in 61% and 75% structural frames. Overall, these findings are greatly consistent with the mCSM-lig server, which ranked the impact of each alanine substitution at different positions. We here concluded from the data shown in Fig. 8 that these three residues are important for substrate recognition and binding as upon the substitution great decline in the binding was observed. To further establish the link between these three residues and the total binding free energy, we used Gibb's free energy and discussed to comprehend further the role of important residue in the binding cavity.

Furthermore, to connect the impact of alanine substitution on substrate binding and estimate and validate the role of these residues in recognizing substrate binding, we calculated MM-GBSA using 5000 structural frames. The total binding energy and its different energy terms were calculated and are presented in Table 3. From Table 3, it can be seen that upon the alanine substitution, the total binding energy decreased. The total binding energy for the wild type was observed to be −48.22 kcal/mol, while for the three mutants V223A, Q346A, and Q514A it was reported to be −39.12 kcal/mol, −35.36 kcal/mol, and −37.29 kcal/mol, respectively. Furthermore, substantial differences in the van der Waals and electrostatic energies were observed. The vdW forces for the wild type, V223A, Q346A, and Q514A were reported to be −66.23 kcal/mol, −56.85.

kcal/mol, −61.21 kcal/mol, and −58.15 kcal/mol, respectively while the electrostatic energies for these complexes were reported as −18.21 kcal/mol, −10.01 kcal/mol, −12.37 kcal/mol, and −15.32 kcal/mol. Overall, these results show that the Q346 may play a significant role in the recognition of substrate. The other residues i.e., V223 and Q514 may also play an essential role in the recognition and binding of substrate.

4. Conclusion

Acetyl-CoA carboxylase (ACC) is considered as one of the target metabolic checkpoints and an attractive drug target against obesity, cancer, microbial infections, and diabetes. Acetyl-CoA carboxylases (ACCs) from actinomycetes have emerged as an important group of enzymes with essential metabolic roles in accordance with the utilization of specific substrates. ACCs with PCC or ACC roles have been biochemically and structurally characterized in *Mycobacterium* and *Streptomyces*. These studies have a great contribution to understanding the ACCs substrate specificity. Other genes encoding CT domains can be recognized in the genome of the disease-causing pathogens, whose physiological role and enzyme activity still awaits elucidation. The CT domain of *S. antibioticus* shares similar structural organization with the previous structures and the two steps reaction was confirmed by enzymatic assay. Furthermore, to reveal the key hotspots required for the substrate recognition and processing, *in silico* mutagenesis validated only three key residues (V223, Q346, and Q514) that help in the fixation of the substrate. Moreover, we also presented atomic level knowledge on the mechanism of the substrate binding, which unveiled the terminal loop (500–514) function as an opening and closing switch and pushes the substrate inside the cavity for stable binding. A significant decline in the hydrogen bonding half-life was observed upon the alanine substitution. Consequently, the presented structural data highlighted the potential key interacting residues for substrate recognition and will also help to re-design ACCs active site for proficient substrate specificity to produce diverse polyketides. The study will also help in designing novel structure-based inhibitors with potential relevance to bacterial infections, obesity, and related metabolic diseases.

Coordinates and structure factors

Coordinates and structure factors are deposited with RCSB PDB under accession code 7W5U.

Table 3
MM-GBSA of wild type, V223A, Q346A, and Q514A mutant systems. All the energies are given in kcal/mol.

Complex Name	MM-GBSA (kcal/mol)			
	Δ_{vdW}	Δ_{elec}	Δ_{ps}	$\Delta_{G\ Total}$
Wild Type	−66.23	−18.21	36.22	−48.22 kcal/mol
V223A	−56.85	−10.01	27.74	−39.12 kcal/mol
Q346A	−61.21	−12.37	38.22	−35.36 kcal/mol
Q514A	−58.15	−15.32	41.53	−37.91 kcal/mol

Declaration of competing interest

Authors declare there is no declaration of interest.

Acknowledgment

We thank the staff of Shanghai Synchrotron Radiation Facility beamlines BL17U and BL18U for access and help with the X-ray data collection. We also thank Dr. Lei Feng of the Instrumental Analysis Center of Shanghai Jiao Tong University for her kind help with LC-MS analysis. This work was supported by the National Key R&D Program of China (2019YFA0905400) and the National Natural Science Foundation of China (32070040).

Appendix A. Supplementary data

Supplementary data to this article can be found online at https://doi.org/10.1016/j.compbiomed.2022.105439.

References

[1] J.E. Cronan Jr., The biotinyl domain of Escherichia coli acetyl-CoA carboxylase: evidence that the "thumb" structure is essential and that the domain functions as a dimer, J. Biol. Chem. 276 (2001) 37355–37364.
[2] F. Zhang, H. Ji, I. Ali, Z. Deng, L. Bai, J. Zheng, Structural and biochemical insight into the recruitment of acyl carrier protein-linked extender units in ansamitocin biosynthesis, Chembiochem 21 (2020) 1309–1314.
[3] L. Diacovich, D.L. Mitchell, H. Pham, G. Gago, M.M. Melgar, C. Khosla, H. Gramajo, S.-C. Tsai, Crystal structure of the β-subunit of acyl-CoA carboxylase: structure-based engineering of substrate specificity, Biochemistry 43 (2004) 14027–14036.
[4] A.L. Livieri, L. Navone, E. Marcellin, H. Gramajo, E. Rodriguez, A novel multidomain acyl-CoA carboxylase in Saccharopolyspora erythraea provides malonyl-CoA for de nov o fatty acid biosynthesis, Sci. Rep. 9 (2019) 1–10.
[5] M.J. Salie, J.J. Thelen, Regulation and structure of the heteromeric acetyl-CoA carboxylase, Biochim. Biophys. Acta Mol. Cell Biol. Lipids 1861 (2016) 1207–1213.
[6] L. Diacovich, S. Peirú, D. Kurth, E. Rodríguez, F. Podestá, C. Khosla, H. Gramajo, Kinetic and structural analysis of a new group of acyl-CoA carboxylases found in Streptomyces coelicolor A3 (2), J. Biol. Chem. 277 (2002) 31228–31236.
[7] M. Bennett, M. Högbom, Crystal structure of the essential biotin-dependent carboxylase AccA3 from Mycobacterium tuberculosis, FEBS Open bio. 7 (2017) 620–626.
[8] X. Yao, D. Wei, C. Soden, M.F. Summers, D. Beckett, Structure of the carboxy-terminal fragment of the apo-biotin carboxyl carrier subunit of Escherichia coli acetyl-CoA carboxylase, Biochemistry 36 (1997) 15089–15100.
[9] H. Zhang, B. Tweel, J. Li, L. Tong, Crystal structure of the carboxyltransferase domain of acetyl-coenzyme A carboxylase in complex with CP-640186, Structure 12 (2004) 1683–1691.
[10] J.D. McGarry, N.F. Brown, The mitochondrial carnitine palmitoyltransferase system—from concept to molecular analysis, Eur. J. Biochem. 244 (1997) 1–14.
[11] X. Zu, J. Zhong, D. Luo, J. Tan, Q. Zhang, Y. Wu, J. Liu, R. Cao, G. Wen, D. Cao, Chemical genetics of acetyl-CoA carboxylases, Molecules 18 (2013) 1704–1719.
[12] H.J. Harwood Jr., Treating the metabolic syndrome: acetyl-CoA carboxylase inhibition, Expert Opin. Ther. Targets 9 (2005) 267–281.
[13] L. Tong, H.J. Harwood Jr., Acetyl-coenzyme A carboxylases: versatile targets for drug discovery, J. Cell. Biochem. 99 (2006) 1476–1488.
[14] G. Gago, L. Diacovich, A. Arabolaza, S.-C. Tsai, H. Gramajo, Fatty acid biosynthesis in actinomycetes, FEMS Microbiol. Rev. 35 (2011) 475–497.
[15] L. Tong, Acetyl-coenzyme A carboxylase: crucial metabolic enzyme and attractive target for drug discovery, CMLS Cell. Mol. Life Sci. 62 (2005) 1784–1803.
[16] L. Abu-Elheiga, H. Wu, Z. Gu, R. Bressler, S.J. Wakil, Acetyl-CoA carboxylase 2−/− mutant mice are protected against fatty liver under high-fat, high-carbohydrate dietary and de novo lipogenic conditions, J. Biol. Chem. 287 (2012) 12578–12588.

[17] L.M. Stunkard, B.J. Kick, J.R. Lohman, Structures of LnmK, a bifunctional acyltransferase/decarboxylase, with substrate analogues reveal the basis for selectivity and stereospecificity, Biochemistry 60 (2021) 365–372.
[18] L. Chen, Y. Duan, H. Wei, H. Ning, C. Bi, Y. Zhao, Y. Qin, Y. Li, Acetyl-CoA carboxylase (ACC) as a therapeutic target for metabolic syndrome and recent developments in ACC1/2 inhibitors, Expet Opin. Invest. Drugs 28 (2019) 917–930.
[19] T. Liu, L. Gou, S. Yan, T. Huang, Inhibition of acetyl-CoA carboxylase by PP-7a exerts beneficial effects on metabolic dysregulation in a mouse model of diet-induced obesity, Exp. Ther. Med. 20 (2020) 521–529.
[20] J.R. Miller, S. Dunham, I. Mochalkin, C. Banotai, M. Bowman, S. Buist, B. Dunkle, D. Hanna, H.J. Harwood, M.D. Huband, A class of selective antibacterials derived from a protein kinase inhibitor pharmacophore, Proc. Natl. Acad. Sci. Unit. States Am. 106 (2009) 1737–1742.
[21] M.A. Silvers, G.T. Robertson, C.M. Taylor, G.L. Waldrop, Design, synthesis, and antibacterial properties of dual-ligand inhibitors of acetyl-CoA carboxylase, J. Med. Chem. 57 (2014) 8947–8959.
[22] M.K. Craft, G.L. Waldrop, Mechanism of biotin carboxylase inhibition by ethyl 4-[[2-chloro-5-(phenylcarbamoyl) phenyl] sulfonylamino] benzoate, J. Enzym. Inhib. Med. Chem. 37 (2022) 100–108.
[23] E. Rodrıguez, C. Banchio, L. Diacovich, M.J. Bibb, H. Gramajo, Role of an essential acyl coenzyme A carboxylase in the primary and secondary metabolism of Streptomyces coelicolor A3 (2), Appl. Environ. Microbiol. 67 (2001) 4166–4176.
[24] A.L. Livieri, L. Navone, E. Marcellin, H. Gramajo, E. Rodriguez, A novel multidomain acyl-CoA carboxylase in Saccharopolyspora erythraea provides malonyl-CoA for de novo fatty acid biosynthesis, Sci. Rep. 9 (2019) 1–10.
[25] D.A. Hopwood, D.H. Sherman, Molecular genetics of polyketides and its comparison to fatty acid biosynthesis, Annu. Rev. Genet. 24 (1990) 37–62.
[26] L. Dong, L.-B. Lü, R. Lai, Molecular Cloning of Tupaia Belangeri Chinensis Neuropeptide Y and Homology Comparison with Other Analogues from Primates, 2012.
[27] A.J. Hughes, A. Keatinge-Clay, Enzymatic extender unit generation for in vitro polyketide synthase reactions: structural and func-tional showcasing of Streptomyces coelicolor MatB, Chem. Biol. 18 (2011) 165–176.
[28] O. Trott, A.J. Olson, AutoDock Vina: improving the speed and accuracy of docking with a new scoring function, efficient optimization, and multithreading, J. Comput. Chem. 31 (2010) 455–461.
[29] K.L. Morrison, G.A. Weiss, Combinatorial alanine-scanning, Curr. Opin. Chem. Biol. 5 (2001) 302–307.
[30] S.M. Simonsen, L. Sando, K.J. Rosengren, C.K. Wang, M.L. Colgrave, N.L. Daly, D. J. Craik, Alanine scanning mutagenesis of the prototypic cyclotide reveals a cluster of residues essential for bioactivity, J. Biol. Chem. 283 (2008) 9805–9813.
[31] A. Khan, M.T. Khan, S. Saleem, M. Junaid, A. Ali, S.S. Ali, M. Khan, D.-Q. Wei, Structural Insights into the mechanism of RNA recognition by the N-terminal RNA-binding domain of the SARS-CoV-2 nucleocapsid phosphoprotein, Comput. Struct. Biotechnol. J. 18 (2020) 2174–2184.
[32] A. Khan, T. Zia, M. Suleman, T. Khan, S.S. Ali, A.A. Abbasi, A. Mohammad, D. Q. Wei, Higher infectivity of the SARS-CoV-2 new variants is associated with K417N/T, E484K, and N501Y mutants: an insight from structural data, J. Cell. Physiol. 10 (2021) 7045–7057.
[33] D.E. Pires, D.B. Ascher, mCSM–NA: predicting the effects of mutations on protein–nucleic acids interactions, Nucleic Acids Res. 45 (2017) W241–W246.
[34] M. Ccgi, Molecular Operating Environment (MOE), 2013.08, Chemical Computing Group Inc., Montreal, 2016.
[35] M. Batool, M. Shah, M.C. Patra, D. Yesudhas, S. Choi, Structural insights into the Middle East respiratory syndrome coronavirus 4a protein and its dsRNA binding mechanism, Sci. Rep. 7 (2017) 1–14.
[36] D.A. Case, T.E. Cheatham III, T. Darden, H. Gohlke, R. Luo, K.M. Merz Jr., A. Onufriev, C. Simmerling, B. Wang, R.J. Woods, The Amber biomolecular simulation programs, J. Comput. Chem. 26 (2005) 1668–1688.
[37] R. Martoňák, A. Laio, M. Parrinello, Predicting crystal structures: the Parrinello-Rahman method revisited, Phys. Rev. Lett. 90 (2003), 075503.
[38] R. Salomon-Ferrer, A.W. Götz, D. Poole, S. Le Grand, R.C. Walker, Routine microsecond molecular dynamics simulations with AMBER on GPUs. 2. Explicit solvent particle mesh Ewald, J. Chem. Theor. Comput. 9 (2013) 3878–3888.
[39] W.L. DeLano, Pymol: an open-source molecular graphics tool, CCP4 Newsl. Protein Crystallogr. 40 (2002) 82–92.
[40] S. Genheden, U. Ryde, The MM/PBSA and MM/GBSA methods to estimate ligand-binding affinities, Expet Opin. Drug Discov. 10 (2015) 449–461.
[41] S.K. Mishra, J. Koča, Assessing the performance of MM/PBSA, MM/GBSA, and QM–MM/GBSA approaches on protein/carbohydrate complexes: effect of implicit solvent models, QM methods, and entropic contributions, J. Phys. Chem. B 122 (2018) 8113–8121.
[42] K.S. Wendt, I. Schall, R. Huber, W. Buckel, U. Jacob, Crystal structure of the carboxyltransferase subunit of the bacterial sodium ion pump glutaconyl-coenzyme A decarboxylase, EMBO J. 22 (2003) 3493–3502.
[43] H. Zhang, Z. Yang, Y. Shen, L. Tong, Crystal structure of the carboxyltransferase domain of acetyl-coenzyme A carboxylase, Science 299 (2003) 2064–2067.
[44] T.-W. Lin, M.M. Melgar, D. Kurth, S.J. Swamidass, J. Purdon, T. Tseng, G. Gago, P. Baldi, H. Gramajo, S.-C. Tsai, Structure-based inhibitor design of AccD5, an essential acyl-CoA carboxylase carboxyltransferase domain of Mycobacterium tuberculosis, Proc. Natl. Acad. Sci. Unit. States Am. 103 (2006) 3072–3077.
[45] P.R. Hall, Y.F. Wang, R.E. Rivera-Hainaj, X. Zheng, M. Pustai-Carey, P.R. Carey, V. C. Yee, Transcarboxylase 12S crystal structure: hexamer assembly and substrate binding to a multienzyme core, EMBO J. 22 (2003) 2334–2347.
[46] P.R. Hall, Y.-F. Wang, R.E. Rivera-Hainaj, X. Zheng, M. Pustai-Carey, P.R. Carey, V. C. Yee, Transcarboxylase 12S crystal structure: hexamer assembly and substrate binding to a multienzyme core, EMBO J. 22 (2003) 2334–2347.
[47] H.M. Holden, M.M. Benning, T. Haller, J.A. Gerlt, The crotonase superfamily: divergently related enzymes that catalyze different reactions involving acyl coenzyme a thioesters, Accounts Chem. Res. 34 (2001) 145–157.
[48] F. Lombó, A.F. Braña, J.A. Salas, C. Méndez, Genetic organization of the biosynthetic gene cluster for the antitumor angucycline oviedomycin in Streptomyces antibioticus ATCC 11891, Chembiochem 5 (2004) 1181–1187.
[49] D.E. Pires, T.L. Blundell, D.B. Ascher, mCSM-lig: quantifying the effects of mutations on protein-small molecule affinity in genetic disease and emergence of drug resistance, Sci. Rep. 6 (2016) 1–8.